Photometric and Spectroscopic Observations of GRB 140629A

Li-Ping Xin[1] , Shu-Qing Zhong[2], En-Wei Liang[2] , Jing Wang[1,3], Hao Liu[1], Tian-Meng Zhang[4], Xiao-Li Huang[2], Hua-Li Li[1],
Yu-Lei Qiu[1], Xu-Hui Han[1], and Jian-Yan Wei[1,3]

[1] CAS Key Laboratory of Space Astronomy and Technology, National Astronomical Observatories, Chinese Academy of Sciences,
Beijing 100012, People's Republic of China; xlp@nao.cas.cn
[2] Guangxi Key Laboratory for Relativistic Astrophysics, School of Physical Science and Technology, Guangxi University,
Nanning 530004, People's Republic of China; lew@gxu.edu.cn
[3] School of Astronomy and Space Science, University of Chinese Academy of Sciences, 19A Yuquan Rd, Shijingshan District,
Beijing 100049, People's Republic of China
[4] Key Laboratory of Optical Astronomy, National Astronomical Observatories, Chinese Academy of Sciences, Beijing 100012, People's Republic of China

Abstract

We present our optical photometric and spectroscopical observations of GRB 140629A. A redshift of $z = 2.275 \pm 0.043$ is measured through the metal absorption lines in our spectroscopic data. Using our photometric data and multiple observational data from other telescopes, we show that its optical light curve is well interpreted with the standard forward shock models in the thin shell case. Its optical–X-ray afterglow spectrum is jointly fitted with a single power-law function, yielding a photon index of -1.90 ± 0.05. The optical extinction and neutral hydrogen absorption of the gamma-ray burst (GRB) host galaxy are negligible. The fit to the light curve with the standard models shows that the ambient density is $60 \pm 9\,\mathrm{cm}^{-3}$ and the GRB radiating efficiency is as low as $\sim 0.24\%$, likely indicating a baryonic-dominated ejecta of this GRB. This burst agrees well with the $L_{p,iso}$–E'_p–Γ_0 relation, but confidently violates those empirical relations involving geometric corrections (or jet break time). This gives rise to an issue of the possible selection effect on these relations since the jet opening angle of this GRB is extremely narrow (0.04 rad).

Key words: gamma-ray burst: individual (140629A) – stars: individual (GRB 140629A) – techniques: photometric – techniques: spectroscopic

1. Introduction

Gamma-ray bursts (GRBs) and their afterglows in soft energy bands are the most luminous events in the deep universe (Mészáros 2006; Kumar & Zhang 2015). Typically, their short gamma-ray flashes may release an amount of isotropic energy in the gamma-ray band ($E_{\gamma,iso}$) of 10^{50}–10^{54} erg within tens of seconds. Their optical emissions may be so bright that some of them can be even occasionally seen with the naked eye, such as GRB 080319B (Racusin et al. 2008). As an expectation of collimated jet models (Harrison et al. 1999; Rhoads 1999; Dai et al. 2007), jet breaks have been detected in the late multi-wavelength afterglow light curves of some bursts (e.g., Nicuesa Guelbenzu et al. 2011), which make their true energy release smaller than the isotropic one by 2–3 orders of magnitude (e.g., Frail et al. 2001; Bloom et al. 2003).

The discovery of the multi-wavelength emission of afterglows has revolutionized our understanding of the GRB phenomenon (e.g., Piran 1999; Zhang & Mészáros 2004). Due to the rapid response and the precise localization capabilities of the X-ray telescope (XRT) on board the *Swift* mission, X-ray afterglows are detected for more than 96% of the GRBs that trigger the *Swift* Burst Alert Telescope (BAT; Burrows et al. 2007). Most of the well-sampled XRT light curves usually start with bright flares and/or a steep decay

segment with a slope[5] of $\alpha < -3$ (Nousek et al. 2006; O'Brien et al. 2006; Zhang et al. 2006). The joint spectral analysis of these X-ray flares with simultaneous gamma-ray pulses indicates that they are the low-energy extension of prompt gamma-ray emission (Peng et al. 2014). The initial steep decay phase is explained as being the tail emission of the last gamma-ray emission pulse due to the so-called curvature effect (e.g., Liang et al. 2006; Zhang et al. 2007; Mu et al. 2016). Following the initial steep decay segment, XRT light curves usually have a shallow decay segment with a slope of $\alpha \sim -0.5$ or even shallower, before transferring to the so-called standard decay segment with a slope of $\alpha \sim -1$. These features well agree with the predictions of external shock models with extra energy injection (Dai & Lu 1998; Zhang & Mészáros 2002; Liang et al. 2007). A jet-like decay segment is only observed in a few XRT light curves (Liang et al. 2008), and a small fraction of XRT light curves are featureless, showing a single power-law flux decay from very early to late epochs (Liang et al. 2009).

Large sample analysis for GRB optical light curves (e.g., Oates et al. 2009; Kann et al. 2010; Panaitescu & Vestrand 2011; Li et al. 2012) shows that a significant fraction of them were found to start with a smooth bump and then decay as a power law. This feature might be due to the deceleration of the GRB fireball by the surrounding medium as predicted by forward shock models in the thin shell case (Sari & Piran 1999; Kobayashi & Zhang 2007). About one-third of their optical

---

[5] The flux convention $F \propto t^{\alpha}\nu^{\beta}$ is adopted, where α and β are the temporal and spectral indices, respectively.

light curves start with a shallow decay segment, as usually seen in XRT light curves (Li et al. 2012). The detection rate of optical flares is much lower than that of X-ray flares (e.g., Li et al. 2012; Swenson et al. 2013). It was proposed that early optical light curves may be good probes for investigating the properties of fireballs and the ambient density (e.g., Liang et al. 2010, 2013; Yi et al. 2013; Xin et al. 2016a). Although the chromatic breaks observed in both X-ray and optical afterglow light curves give rise to an issue in explaining their physical origins (Fan & Piran 2006; Panaitescu et al. 2006; Liang et al. 2007), X-ray and optical data can be accommodated within the external shock models by considering various effects (e.g., Cucchiara et al. 2011; Wang et al. 2015a).

In this paper, we report our optical photometric and spectroscopical observations of GRB 140629A with the TNT (0.8 m Tsinghua University—National Astronomical Observatory of China Telescope) and the 2.16 m telescope at Xinglong Observatory. We show that these observations are consistent with the prediction of the external shock fireball model in the thin shell case. Combining our data with other observations carried out by *Swift*, *Konus-Wind*, and other ground-based telescopes, we derive the jet properties of this GRB and examine whether it satisfies empirical relations derived from observations of both the prompt gamma-rays and the afterglows. Our observations and data reduction are presented in Section 2. The analysis of the spectroscopical data and the redshift measurement of GRB 140629A are reported in Section 3. The analysis of the optical and X-ray afterglow photometric data and our modeling of the afterglow light curves are reported in Section 4. A discussion of our results and our conclusions are presented in Sections 5 and 6. A standard cosmology model with $H_0 = 70 \, \mathrm{km \, s^{-1} \, Mpc^{-1}}$, $\Omega_M = 0.27$, and $\Omega_\Lambda = 0.73$ is adopted. The notation $Q_n = Q/10^n$ is in cgs units.

2. Observations and Data Reduction

2.1. Prompt Gamma-Ray Emission and X-Ray Afterglow Observations

GRB 140629A triggered the *Swift* BAT at 14:17:30 UT on 2014 June 29 (T_0; Lien et al. 2014). It was also detected by *Konus-Wind* in the waiting mode (Golenetskii et al. 2014). The BAT light curve starts with weak and overlapped emission peaks prior to the BAT trigger of about 8 s and ends at about 90 s post trigger time with some fluctuations (Cummings et al. 2014), as observed in some long BAT GRBs (Hu et al. 2014). The burst duration (T_{90}) is 42.0 ± 14.3 s measured in the BAT 15–150 keV energy band (Cummings et al. 2014). Its duration measured by *Konus-Wind* in the energy range from 20 to 10,000 keV is less than 26 s (Golenetskii et al. 2014), being much shorter than that in the BAT band. This confirms that the duration of the GRB prompt emission depends on the instrument energy band (e.g., Qin et al. 2013). The time-integrated, prompt gamma-ray spectrum observed with *Konus-Wind* in the $20-10^4$ keV band can be best fitted with a cutoff power-law function, yielding a photon index of $\Gamma_\gamma = -1.42 \pm 0.54$ and a peak energy of the νf_ν spectrum of $E_p = 86 \pm 17$ keV. The associated gamma-ray fluence and the peak flux are $S_\gamma = (3.4 \pm 0.5) \times 10^{-6} \, \mathrm{erg \, cm^{-2}}$ and $F_\gamma = (4.7 \pm 0.7) \times 10^{-7} \, \mathrm{erg \, cm^{-2} \, s^{-1}}$, respectively (Golenetskii et al. 2014). The X-ray afterglow was detected by XRT at a time $t > T_0 + 93$ s, roughly at the end of the prompt emission.
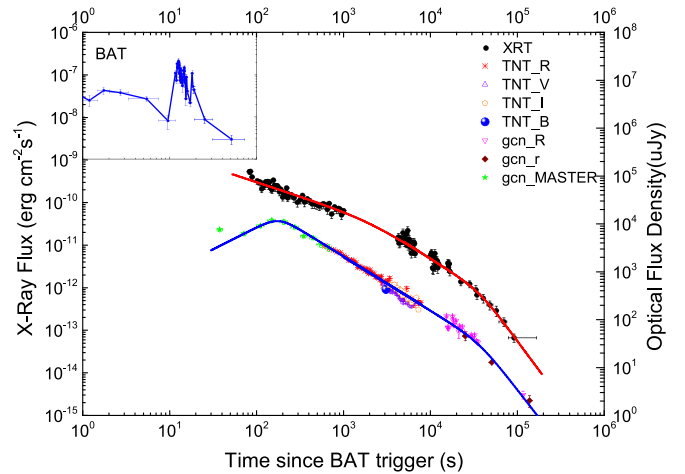

Figure 1. Multi-wavelength light curves of GRB 140629A and our empirical fits to the *R* band and X-ray light curves with smooth broken power laws.

We obtain the BAT and the XRT light curves from the XRT light curve and spectral repository (Evans et al. 2007, 2009).[6] As shown in Figure 1, the prompt gamma-rays show two episodes. The first lasts from $T_0 - 8$ s to $T_0 + 10$ s; the second is from $T_0 + 10$ s to $T_0 + 90$ s.

2.2. Photometric Observations of the Optical Afterglows

The bright optical counterpart of GRB 140629A was detected by several ground-based telescopes, such as the three MASTER system telescopes located in Blagoveshchensk, Tunka, and Kislovodsk (Gorbovskoy et al. 2014; Yurkov et al. 2014), the Russian–Turkish 1.5 m telescope (Bikmaev et al. 2014), the 1.05 m Schmidt telescope at Kiso Observatory in Japan (Maehara 2014), the Murikabushi 1 m telescope of the Ishigakijima Astronomical Observatory (Kuroda et al. 2014), the Nordic Optical Telescope, and the Palomar 60 inch (P60) robotic telescope (Perley & Cenko 2014).

Our optical follow-up observation campaign of GRB 140629A was carried out using the TNT, beginning at $T_0 + 581$ s and ending at about 2.15 hr after the *Swift*/BAT trigger time. Several *B*-, *V*-, *R*-, and *I*-band images were obtained. The data reduction was carried out following the standard routine in the IRAF[7] package, including bias and flat-field corrections. Dark correction was not performed since its impact on the source extraction and photometry was negligible once the CCD was cooled down to $-110°C$. A point-spread function photometry method was applied via the DAOPHOT task in the IRAF package. During the reduction, *B*-band frames were stacked in order to increase the signal-to-noise ratio (S/N). An absolute photometric calibration was performed using the Sloan Digital Sky Survey (SDSS, Adelman-McCarthy et al. 2008), with flux/mag conversion of the SDSS system into the Johnson–Cousins system.[8] All the data we obtained using the TNT are presented in Table 1. For more details of the follow-up system of the TNT and the data reduction, refer to Zheng et al. (2008) and Xin et al. (2011).

---

[6] http://www.swift.ac.uk/
[7] IRAF is distributed by NOAO, which is operated by AURA, Inc., under cooperative agreement with NSF.
[8] http://www.sdss.org/dr6/algorithms/sdssUBVRITransform.html #Lupton2005.

Table 1
Optical Afterglow Photometry Log[a] of GRB 140629A by TNT

$T-T_0$	Exposure	Filter	Mag	σ	$T-T_0$	Exposure	Filter	Mag	σ
3087	40	B	17.47	0.18	2722	60	R	16.46	0.08
2950	40	V	17.05	0.15	2800	60	R	16.76	0.10
3308	60	V	17.17	0.11	2878	60	R	16.94	0.11
3471	60	V	17.40	0.12	3077	40	R	16.71	0.11
3633	60	V	17.42	0.10	3251	40	R	16.69	0.10
3795	60	V	17.33	0.08	3414	40	R	16.55	0.11
3957	60	V	17.41	0.08	3576	40	R	16.94	0.08
4120	60	V	17.55	0.09	3738	40	R	17.04	0.08
4272	60	V	17.58	0.09	3901	40	R	16.91	0.07
4424	60	V	17.65	0.09	4063	40	R	17.23	0.09
4577	60	V	17.80	0.11	4215	40	R	17.12	0.07
4729	60	V	17.84	0.12	4368	40	R	17.23	0.08
4881	60	V	17.98	0.12	4520	40	R	17.21	0.08
5044	80	V	17.81	0.10	4672	40	R	17.39	0.09
5216	80	V	17.97	0.11	4824	40	R	17.40	0.09
5408	80	V	17.88	0.09	4977	40	R	17.60	0.11
5600	80	V	17.81	0.10	5149	40	R	17.55	0.10
5813	80	V	18.13	0.13	5341	40	R	17.09	0.14
6025	80	V	18.15	0.14	5534	40	R	17.73	0.19
6247	100	V	18.04	0.12	5736	60	R	17.81	0.12
6529	100	V	17.93	0.12	5948	60	R	17.65	0.10
611	60	R	14.85	0.02	6160	60	R	17.76	0.11
690	60	R	14.99	0.03	6433	80	R	17.95	0.12
768	60	R	15.07	0.03	6715	80	R	17.70	0.12
846	60	R	15.16	0.03	7027	100	R	17.73	0.12
924	60	R	15.22	0.03	7407	120	R	17.84	0.13
1003	60	R	15.37	0.03	7729	200	R	17.83	0.09
1081	60	R	15.47	0.03	3367	40	I	16.56	0.10
1159	60	R	15.61	0.04	3529	40	I	16.55	0.08
1237	60	R	15.59	0.03	3691	40	I	16.63	0.09
1315	60	R	15.64	0.04	3854	40	I	16.53	0.07
1393	60	R	15.75	0.05	4016	40	I	16.75	0.08
1471	60	R	15.97	0.05	4173	30	I	16.70	0.09
1549	60	R	15.93	0.04	4326	30	I	16.81	0.09
1628	60	R	16.01	0.04	4478	30	I	16.94	0.10
1706	60	R	16.04	0.05	4630	30	I	16.83	0.10
1784	60	R	16.15	0.05	4783	30	I	17.10	0.12
1862	60	R	16.06	0.05	4935	30	I	16.93	0.11
1940	60	R	16.29	0.06	5107	30	I	17.07	0.12
2018	60	R	16.12	0.05	5482	50	I	17.29	0.11
2096	60	R	16.27	0.06	5674	50	I	17.26	0.12
2175	60	R	16.30	0.07	5886	50	I	17.22	0.11
2253	60	R	16.34	0.07	6099	50	I	17.46	0.14
2331	60	R	16.46	0.08	6346	80	I	17.35	0.10
2409	60	R	16.47	0.07	6628	80	I	17.29	0.11
2487	60	R	16.49	0.08	6930	80	I	17.21	0.12
2566	60	R	16.53	0.07	7290	100	I	17.84	0.23
2644	60	R	16.61	0.09	…	…	…	…	…

Note.

[a] The reference time T_0 is *Swift*/BAT burst trigger time. "$T-T_0$" is the middle time in seconds. "Exposure" is the exposure time in seconds. "σ" means the uncertainty of magnitude. All data are calibrated by nearby SDSS reference stars. No data are corrected for Galactic extinction (which is $E_{B-V} = 0.01$, Schlegel et al. 1998).

A well-sampled optical light curve is obtained from our observations from $T_0 + 580$ s to $T_0 + 2.15$ hr. In order to get an optical light curve in broader temporal coverage, we collect the early and late optical observations of the other telescopes from GCN Circulars (Bikmaev et al. 2014; Gorbovskoy et al. 2014, Malesani 2014; Masi 2014; Moskvitin et al. 2014b, 2014c; Perley & Cenko 2014; Sonbas et al. 2014). Note that the early optical data observed with the MASTER system telescopes were also re-calibrated to USNO B1.0 R2 mag as done for our

observations. During $t \sim 600$–800 s after the burst trigger, simultaneous observations with the MASTER system and our TNT telescope were available. We found that the corrected magnitudes derived from the data observed with the MASTER system were systematically brighter than TNT data by $\Delta R = 0.51$ mag. The discrepancy might be caused by the flux calibration between the two telescopes. We therefore re-normalized the MASTER data to the TNT data by adding $\Delta R = 0.51$ mag based on the simultaneously observed data

during $t \sim 600$–800 s after the burst. We finally obtained an optical light curve covering a duration from $T_0 + 38$ s to $T_0 + 1.4 \times 10^5$ s, as shown in Figure 1.

2.3. Spectroscopic Observations of the Optical Afterglows

We carried out spectroscopic observations with the National Astronomical Observatories, Chinese Academy of Sciences (NAOC) 2.16 m telescope (Fan et al. 2016) in Xinglong Observatory on 2014 June 29 at 15:10:48 (UT), about one hour after the burst trigger. The optical spectrum was obtained with an Optomechanics Research Inc. spectrograph. The spectrograph was equipped with a back-illuminated SPEC 1340×400 CCD. The grating was 300 g mm^{-1}, and the slit oriented in the south–north direction corresponded to a width of $2''0$. This setup finally resulted in a spectral resolution of ~ 9 Å, as measured from the sky emission lines and comparison arcs. The spectrum was blazed at a wavelength of 6000 Å, and was obtained with an exposure time of 2400 s. The two-dimensional spectrum was reduced by the standard procedures in the IRAF package, including bias subtraction, flat-field correction, and cosmic ray removal before the extraction of the one-dimensional spectrum. The extracted one-dimensional spectrum was then calibrated in wavelength by the helium–neon–argon comparison arc taken immediately after the exposure. The subsequent resulting wavelength accuracy was better than 1 Å. The calibration in flux was carried out by the Kitt Peak National Observatory standard stars BD+332642 (Massey et al. 1988). The two telluric features at around $\lambda 6800$ and $\lambda 7600$ due to O_2 molecules were removed from the observed spectrum by the standard calibration stars.

3. Redshift Measurement and Optical Spectrum Features

In order to enhance the S/N, the spectrum was smoothed by a box size of 3 Å. The reduced spectrum in the observer frame is shown in Figure 2. By excluding the artificial features due to the poor subtraction of the night sky emission, a series of hydrogen and metal absorption (Lyα, C II$\lambda 1335$, Si IV$\lambda\lambda 1394,1403$, C IV$\lambda 1549$ and Al II$\lambda 1671$) are identified from the optical spectrum. The redshift of GRB 140629A is determined through the metal absorptions because of the damped Lyα absorption and the poor S/N at the blue end. We finally obtain a redshift of $z = 2.275 \pm 0.043$, in which the wavelength of each line center in the observer frame is estimated by a line profile modeling method using a Gaussian function. Our result is consistent with those reported by other groups (D'Avanzo et al. 2014; Moskvitin et al. 2014a).

Based on our estimated redshift, we derive the optical spectrum in the rest-frame. Correction for Galactic extinction is applied using a color excess $E(B - V)$ taken from the NASA/IAPC Extragalactic Database, assuming $R_V = 3.1$ (Cardelli et al. 1989). We model each absorption feature in the rest-frame by a Gaussian profile through the IRAF/SPECFIT package task (Kriss 1994), except for the damped Lyα absorption. Our results are illustrated in Figure 2. The measured equivalent widths (EWs) in the rest-frame are reported in Table 2. The uncertainties given in Table 2 only include the statistical errors resulting from the spectral fitting. One can observe that the strongest metal absorption occurs in C IV$\lambda 1549$, which is consistent with previous statistical studies based on low-resolution afterglow spectroscopy (e.g., de Ugarte Postigo et al. 2012). The ratio between C IV$\lambda 1549$ and C II$\lambda 1335$ is a

good indicator of ionization by the GRB's intense radiation. The inferred ratio EW(C IV)/EW(C II) is 2.79 ± 0.49, which is higher than the reported average value by a factor of 2 (see Table 8 in de Ugarte Postigo et al. 2012). The variation of the fine structure of the ions has been already observed in several GRBs (e.g., Vreeswijk et al. 2007; D'Elia et al. 2009). Dessauges-Zavadsky et al. (2006) reported a significant decrease of Fe II$\lambda 2396$ transition by a factor of 5 in the afterglow spectrum of GRB 020813. The high ionization revealed in the early afterglow spectrum of GRB 140629A one hour after the burst trigger could be due to a temporal evolution of the ionization as long as the GRB afterglow radiation.

4. Optical and X-Ray Afterglow Data Analysis

4.1. Temporal Analysis

Figure 1 shows the multi-wavelength light curves of GRB 140629A. The first optical data before 650 s after the burst trigger time can be attributed to the prompt emission in the optical band or the reverse shock emission, similar to that observed in GRB 140512A (Huang et al. 2016). We exclude these data in our following analysis.

We fit the optical and X-ray afterglow light curves with a multiple broken power-law model. Each broken power-law function is described as (Beuermann et al. 1999)

$$F = F_0 \left[\left(\frac{t}{t_b} \right)^{\omega \alpha_1} + \left(\frac{t}{t_b} \right)^{\omega \alpha_2} \right]^{1/\omega}, \qquad (1)$$

where t_b is the break time, α_1 and α_2 are decay indices before and after the break, respectively, and ω describes the sharpness of the break, which is fixed as 3 in our analysis. Our empirical fits are illustrated in Figure 1, and summarized in Table 3.

Note that by analyzing the UVOT data of 27 *Swift* GRBs, Oates et al. (2009) report that three GRBs show clear bumps in their UVOT light curves. The rising slopes of these three GRBs are in the range from 0.26 ± 0.13 to 0.73 ± 0.14 before 500 s after the bursts. The UVOT light curves decay with a slope ranging from -0.5 ± 0.05 to -1.67 ± 0.15 after 500 s post the BAT trigger. They proposed that the rise in the optical light curves may be attributed to either the start of the forward shock, or to an off-axis viewing angle where the observer sees an increasing amount of emission as the Lorentz factor of the jet decreases. By analyzing a sample of 17 GRBs with early bumps in their early optical light curves, Liang et al. (2010) showed that the peak time of the early bump is in the range 10^2–10^3 s with a median value of ~ 380 s, and their rising slope r is in the range 1–2, except for three exceptional GRBs: GRB 080330A with $r \sim 0.34$, GRB 060607A with $r \sim 4.15$, and GRB 050820A with $r \sim 4.45$. Their decay slopes are distributed in the range of 0.44–1.77, with an average of 1.16 ± 0.34. Liang et al. (2010) suggested that these bumps could be interpreted as the onset of the forward shock emission and the peak time is the deceleration time of the fireball. For GRB 140629A, we have $\alpha_{O,1} = 0.92 \pm 0.24$, $t_{O,p} = 179 \pm 16$ s, and $\alpha_{O,2} = -1.12 \pm 0.02$, indicating that the early smooth optical peak could be also attributed to the afterglow onset when the GRB fireball is decelerated by the ambient medium (e.g., Sari & Piran 1999; Liang et al. 2010). The optical light curve transits to a steeper segment with $\alpha_{O,3} = -2.35 \pm 0.24$ at $t_{O,j} \sim 37$ ks.
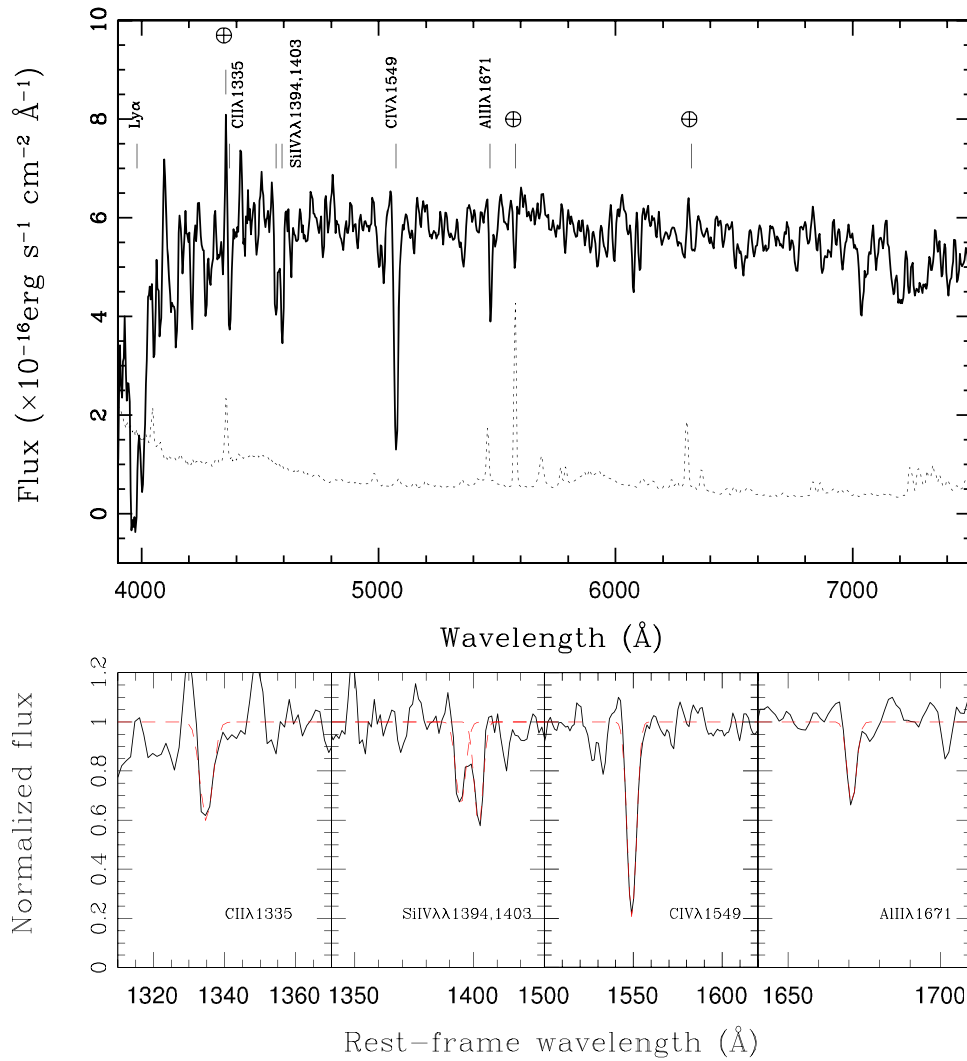
Figure 2. Top: optical spectrum of GRB 140629A (the solid curve) obtained with the Xinglong 2.16 m telescope at about 1 hr after the burst trigger. The spectrum is smoothed by a box size of 3 Å. The dashed curve illustrates the night sky emission spectrum. The identified features both from the GRB afterglow and from the poor subtraction of the night sky emission are marked. Bottom: line modelings with a Gaussian function for the five identified absorption features in the rest-frame. In each panel, the normalized observed spectrum and the best-fit model are shown by the black solid line and by the red dashed line, respectively.

Table 2
Measured EWs in the Rest Frame from the Afterglow
Spectrum of GRB 140629A

Line Identification	Central Wavelength Å	EW Å
C II	1335	1.80 ± 0.31
Si IV	1394	1.74 ± 0.25
Si IV	1403	2.01 ± 0.25
C IV	1549	5.02 ± 0.21
Al II	1671	1.28 ± 0.30

The X-ray afterglow light curve starts with a shallow decay segment with a slope of $\alpha_{X,1} = -0.67 \pm 0.02$ up to $t_{X,b} \sim 2$ ks, which very smoothly transits to a decay slope of $\alpha_{X,2} = -1.31 \pm 0.08$ until a break at $t_{X,j} = 37.2 \pm 9.1$ ks. The decay slope after $t_{X,j}$ is $\alpha_{X,3} = -2.76 \pm 0.40$. The decaying behavior of the X-ray light curve after $t > 200$ s is consistent with the optical light curve.

Achromatic breaks in the optical and X-ray bands are usually suspected to be produced by the jet effect (Rhoads 1999) or the end of energy injection (e.g., Dai & Lu 1998; Liang et al. 2007). A jet break is featured as transition from a normal decay segment with a slope of ~ -1 to a steep decay with a slope of ~ -2. An energy injection break is usually illustrated as transition from a shallow decay segment with a slope of ~ -0.5 to a normal decay segment with a slope of ~ -1. The achromatic break of the optical and X-ray afterglow light curves of GRB 140629A at ~ 37 ks is consistent with the jet break scenario. The decay slope after the break time depends on the index of the electron energy distribution p. We have $\alpha_{O,3} = -2.35 \pm 0.24$ and $\alpha_{X,3} = -2.76 \pm 0.40$, likely suggesting a steep electron spectrum. The large change in slopes around the break time, i.e., $|\Delta\alpha_O| \sim 1.23$ and $|\Delta\alpha_X| \sim 1.43$, also excludes the possibilities of the spectral regime transition, end of energy injection, or medium density drop to making such a break. The transition of the cooling frequency across the band predicts the change of the slopes is $\Delta\alpha = 0.25$ (Sari et al. 1998). The cessation of the energy injection process observed in long GRBs typically leads to $\Delta\alpha \sim 0.7$ (Nousek et al. 2006;

Table 3
Fitting Results of the Multi-wavelength Afterglow Light Curves of GRB 140629A

Band	α_1	α_2	α_3	t_p(s)	t_b(ks)	t_j(ks)	χ^2/dof
Optical	0.92 ± 0.24	-1.12 ± 0.02	-2.35 ± 0.24	179 ± 16	$\cdots$	37.2 (fixed)	8.90^*
X-ray	-0.67 ± 0.02	-1.31 ± 0.08	-2.76 ± 0.40	$\cdots$	2 (fixed)	37.2 ± 9.1	1.06

Note. Note that the value of χ^2/dof for optical data labeled by a star (*) in this table is slightly large, due to the bad fitting of the late optical data. If the fitting were only made to the optical data before 10^4 s after the burst trigger time, the value of χ^2/dof would be ~ 2.20.

Zhang et al. 2006; Liang et al. 2007). A steep drop in the density of the external medium is predicted to cause maximum changes of $\Delta\alpha \sim 0.4$ for density contrasts of ~ 10 (Nakar & Granot 2007).

4.2. Optical–X-Ray Afterglow Spectrum

Multi-wavelength data are available in the time interval from $T_0 + 3084$ s to $T_0 + 7000$ s. We construct the time-averaged broadband afterglow spectrum of GRB 140629A from this time interval. Our optical data are corrected for Galactic foreground extinction with $A_I = 0.012$, $A_R = 0.018$, $A_V = 0.022$ and $A_B = 0.029$. The XRT spectrum is obtained from the XRT light curve and spectral repository (Evans et al. 2007, 2009). It is regrouped to ensure at least 20 counts per bin using the tool "grppha" in Xspec package. We fit the spectrum with a model zdust*zpha*-pha*powerlaw by using the Xspec package, where "zdust" is for the dust extinction of the GRB 140629A host galaxy, "zpha" and "pha" are for the neutral hydrogen absorption of the GRB host galaxy and our Galaxy, respectively, and "powerlaw" is a single power-law function. We find that optical extinction is negligible even when the extinction laws of the Galaxy and the Small and Large Magellanic Clouds were used in our fit. The neutral hydrogen absorption of the GRB host galaxy is also negligible. The absorption of the Galaxy with $N_H = 9.32 \times 10^{19}$ cm^{-2} is adequate to address the observed soft X-ray absorption. The spectrum is well fitted by our model with a $\chi^2/\mathrm{dof} = 31.68/33$, where 33 is the degrees of freedom, as shown in Figure 3. The derived photon index is $\Gamma_{OX} = -1.90 \pm 0.05$.

4.3. Afterglow Light Curve Fits with the External Shock Model

In the framework of the standard afterglow model (e.g., Sari et al. 1998; Huang et al. 2000; Yost et al. 2003), multi-wavelength emission is radiated via the synchrotron process by relativistic electrons accelerated in forward shocks when the fireball propagates into the circumburst medium. For a constant density medium, the typical synchrotron emission frequency, the cooling frequency and the peak spectral flux evolved with time are given by (Sari et al. 1998; Yost et al. 2003; Fan & Piran 2006; Zhang et al. 2007)

$$\nu_m = 3.3 \times 10^{12}\ \mathrm{Hz} \left(\frac{p-2}{p-1}\right)^2 (1+z)^{1/2}$$
$$\times\ \epsilon_{B,-2}^{1/2} \epsilon_{e,-1}^2 E_{K,52}^{1/2} t_d^{-3/2} \tag{2}$$

$$\nu_c = 6.3 \times 10^{15}\ \mathrm{Hz}(1+z)^{-1/2}(1+Y)^{-2}$$
$$\times\ \epsilon_{B,-2}^{-3/2} E_{K,52}^{-1/2} n^{-1} t_d^{-1/2} \tag{3}$$

$$F_{\nu,\mathrm{max}} = 1.6\ \mathrm{mJy}(1+z) D_{28}^{-2} \epsilon_{B,-2}^{1/2} E_{K,52} n^{1/2} \tag{4}$$

where t_d is the observer's time in days, Y is the inverse Compton parameter, D is the luminosity distance, ϵ_e is the fraction of the shock energy in radiating electrons, ϵ_B is the
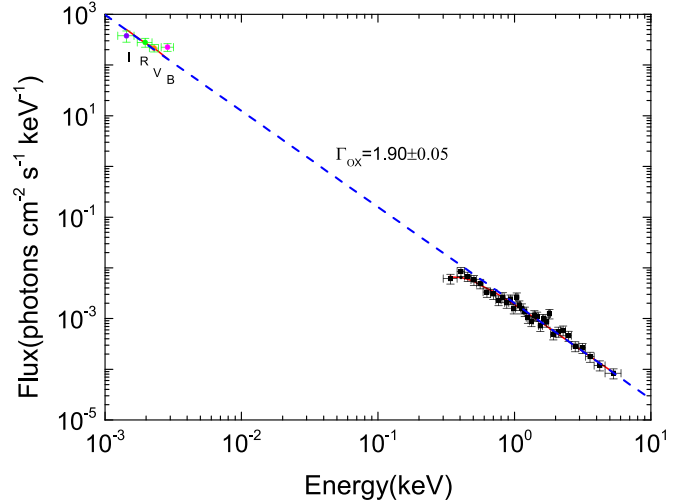

Figure 3. Joint averaged optical–X-ray spectral energy distribution of the afterglow of GRB 140629A derived from the time interval from 3084 to 7000 s after the BAT trigger. The frequencies are expressed in the observer frame. The red solid line is our fitting curve of the broadband spectrum. The blue dashed line is the intrinsic radiation spectrum derived from our fit.

fraction of the shock energy in magnetic fields, n is the medium density, $E_{K,\mathrm{iso}}$ is the isotropic kinetic energy, p is the power-law index of the electron distribution, and z is the redshift.

The standard GRB afterglow model discussed above is adopted in our modeling to derive the properties of the ejecta. We also consider the jet opening angle effect. For GRB 140629A, the optical flux decay slope after the early peak is $\alpha_{O,2} = -1.12 \pm 0.02$. During this decay segment, the derived photon index is $\Gamma_{OX} = -1.90 \pm 0.05$. These values are consistent with the closure relation $\alpha = 3\beta/2$ (Zhang et al. 2006), where $\beta = \Gamma + 1$; thus we can infer that both optical and X-ray afterglows are likely in the synchrotron radiation spectral regime of $\nu_m < \nu_O < \nu_X < \nu_c$ in the slow cooling case for the interstellar medium (ISM) scenario (e.g., Sari et al. 1998; Zhang et al. 2006; Gao et al. 2013). In this spectral regime the observed energy flux is given by

$$\nu F_\nu = F_{\nu,\mathrm{max}}(\nu_m/\nu_X)^{(p-1)/2} \tag{5}$$

and one can also infer $p = -2\beta_{OX} + 1 \sim 2.80$, where $\beta_{OX} = \Gamma_{OX} + 1$ (e.g., Sari et al. 1998; Zhang et al. 2006).

There are seven free parameters in our model, i.e., ϵ_e, ϵ_B, n, $E_{K,\mathrm{iso}}$, p, the jet opening angle (θ_j), and the initial Lorentz factor (Γ_0). Y is not an independent parameter, and whose treatment is the same as in Fan & Piran (2006). To constrain these parameters, a Monte Carlo method is utilized to search for the best-fit parameter set. Following the technique and the procedure (Xin et al. 2016b), the fitting results for GRB 140629A are illustrated in Figure 4, and the derived parameters and their probability distribution are shown in Figure 5. The 1σ confidence levels estimated for the micro-physical parameters are $\Gamma_0 = 315^{+44}_{-34}$,
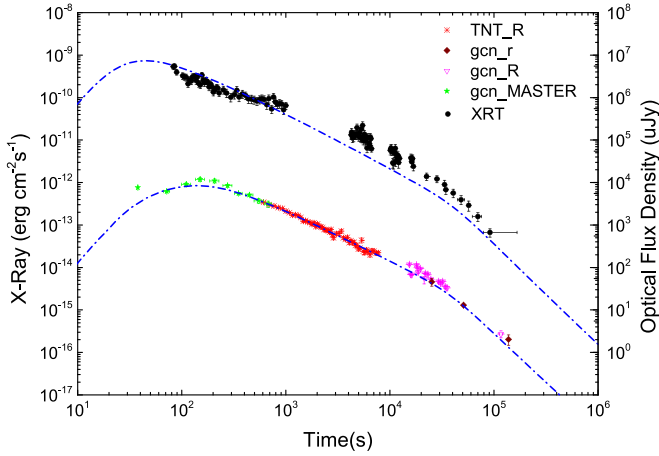
Figure 4. Modeling of the optical and X-ray afterglow light curves with the synchrotron external shock model (blue dashed lines). The derived best micro-physical parameters are: $\Gamma_0 = 315^{+44}_{-34}$, $\epsilon_e = (1.2 \pm 0.1) \times 10^{-2}$, $\epsilon_B = (1.0 \pm 0.1) \times 10^{-6}$, $n = 60 \pm 9$ cm^{-3}, $E_{K,\mathrm{iso}} = (1.8 \pm 0.1) \times 10^{55}$ erg, $p = 2.72 \pm 0.07$, and $\theta_j = 0.04^{+0.02}_{-0.01}$ rad.

$\epsilon_e = (1.2 \pm 0.1) \times 10^{-2}$, $\epsilon_B = (1.0 \pm 0.1) \times 10^{-6}$, $n = 60 \pm 9$ cm^{-3}, $E_{K,\mathrm{iso}} = (1.8 \pm 0.1) \times 10^{55}$ erg, $\theta_j = 0.04^{+0.02}_{-0.01}$ rad, and $p = 2.72 \pm 0.07$.

The derived ϵ_B value is smaller than the typical values of $10^{-2} \sim 10^{-4}$ reported in the literature prior to the *Swift* mission era (e.g., Wijers & Galama 1999; Panaitescu & Kumar 2002; Yost et al. 2003; Panaitescu 2005). Some recent statistical analysis working with both optical and X-ray afterglow data suggests a low ϵ_B value, i.e., $\sim 10^{-8}$–10^{-3} (Japelj et al. 2014; Santana et al. 2014; Gao et al. 2015; Wang et al. 2015b). Note that both optical and X-ray afterglows are in the spectral regime $\nu < \nu_c$ in our modeling fit for GRB 140629A. From Equation (3), ν_c is proportional to $\epsilon_{B,-2}^{-3/2} n^{-1} t_d^{-1/2}$. As time increases, ν_c becomes smaller. One also finds that ν_c is more sensitive to ϵ_B. For GRB 140629A, the derived n value is 60 ± 9 cm^{-3}. In such a dense medium, the extremely low ϵ_B could ensure that both the optical and X-ray emission are still in the regime $\nu < \nu_c$ at late epoch.

The model gives only a rough fit to the X-ray light curve. Note that our best empirical fit to the X-ray light curve derived a shallow decay segment with a slope of -0.67 ± 0.02 before $t < 2 \times 10^3$ s. However, we do not find a similar feature in the optical light curve. We suspect that the shallow decaying behavior may partially result from the tail emission of the prompt gamma-rays of the second episode since the early X-ray emission was observed with XRT starting at 93 s after the BAT trigger, roughly at the end of this episode. Therefore, we do not consider any late energy injection in our modeling fit. In addition, significant flickering is observed in the X-ray light curve. This is a residual of late internal emission, and it is difficult to depict its temporal details.

As shown in Figure 4, the optical data at $t > 300$ s are well represented by our model, but around the onset peak they slightly deviate from it. Our empirical fit for GRB 140629A yields $\alpha_{O,1} = 0.92 \pm 0.24$, which is much shallower than the predicted value of 3 by the model (e.g., Gao et al. 2013) in the thin shell case for a constant medium density. One possibility to explain the shallower rising slope is the temporal evolution of the medium density profile. Liang et al. (2013) found that the

rising slope of the early afterglow onset is shallower than the prediction of a constant medium density for a large fraction of GRBs in their sample. They considered a circumburst medium density profile as

$$n = \begin{cases} n_0 \left(\dfrac{R}{R_t} \right)^{-k}, & R <= R_t, \\ n_0, & R > R_t, \end{cases} \qquad (6)$$

where R_t is the transition radius at which the medium turns into a constant density medium n_0. If the condition $R_t \geqslant R_{\mathrm{dec}}$ is satisfied, where R_{dec} is the deceleration radius, the thin shell external shock model gives a rising slope of $\alpha = 3 - k(p+5)/4$. They derived a typical k value as 1. As mentioned above, $p \sim 2.7$; we then have $\alpha = 1.07$ for GRB 140629A in this scenario. This value is consistent with that derived from our empirical fit within the error bars. On the other hand, for the light curves after the peak time, it is also noticed that the decay index and the spectral slope are consistent with the closure relation, $\alpha = 3\beta/2$ (Zhang et al. 2006) in the slow cooling case for the ISM scenario, indicating that the density profile of the medium after the peak is constant, $k = 0$. As a result, the k parameter before and after the peak time is changed from ~ 1 to 0. Consequently, the transition radius R_t may be similar to the deceleration radius R_{dec}. This is also similar to that in GRB 121011A (Xin et al. 2016a).

Another possibility to interpret the shallow rising slope of the afterglow onset would be contamination of the prompt optical emission or reverse shock emission. As mentioned in Section 4.1, the first optical data may be dominated by either of these (see also in GRB 140512A; Huang et al. 2016). The early forward shock emission may contaminated by the prompt optical and/or reverse shock emission. If the emission from the reverse shock and the forward shock at the early rising phase are comparable, the contamination effect would cause a significant surplus in comparison with the prediction of the forward shock model.

5. Discussion

The GRB radiative efficiency (η_γ) is of theoretical interest since it may provide some hints as to the composition of the ejecta. With the measured redshift, $z = 2.275$, the isotropic energy release $E_{\gamma,\mathrm{iso}}$ is estimated to be 4.4×10^{52} erg using observed S_γ in the 20–10^4 keV band. Therefore, we have $\eta_\gamma = E_{\gamma,\mathrm{iso}}/(E_{K,\mathrm{iso}} + E_{\gamma,\mathrm{iso}}) = 0.24\%$. This is extremely low in comparison with the typical GRBs shown in Figure 6 (see also Zhang et al. 2007). It was suggested that the GRB radiation efficiency is low in the keV–MeV band, if the radiation is produced by the internal shocks in collisions of ultra-relativistic matter shells (e.g., Kobayashi et al. 1997; Daigne & Mochkovitch 1998; Kumar 1999; Panaitescu et al. 1999).[9] The derived low efficiency is consistent with the prediction of the standard internal shock model.

For GRB 140629A, our analysis suggests that the optical and X-ray afterglows are from a narrow jet ($\theta_j = 0.04^{+0.02}_{-0.01}$ rad) with a low ϵ_B [$(1.0 \pm 0.01) \times 10^{-6}$] in a dense medium

---

[9] The radiation efficiency may be much higher ($\sim 40\%$) when the inner engine produces fireball shells with comparable energies but with very different Lorentz factors (Kobayashi et al. 1997).
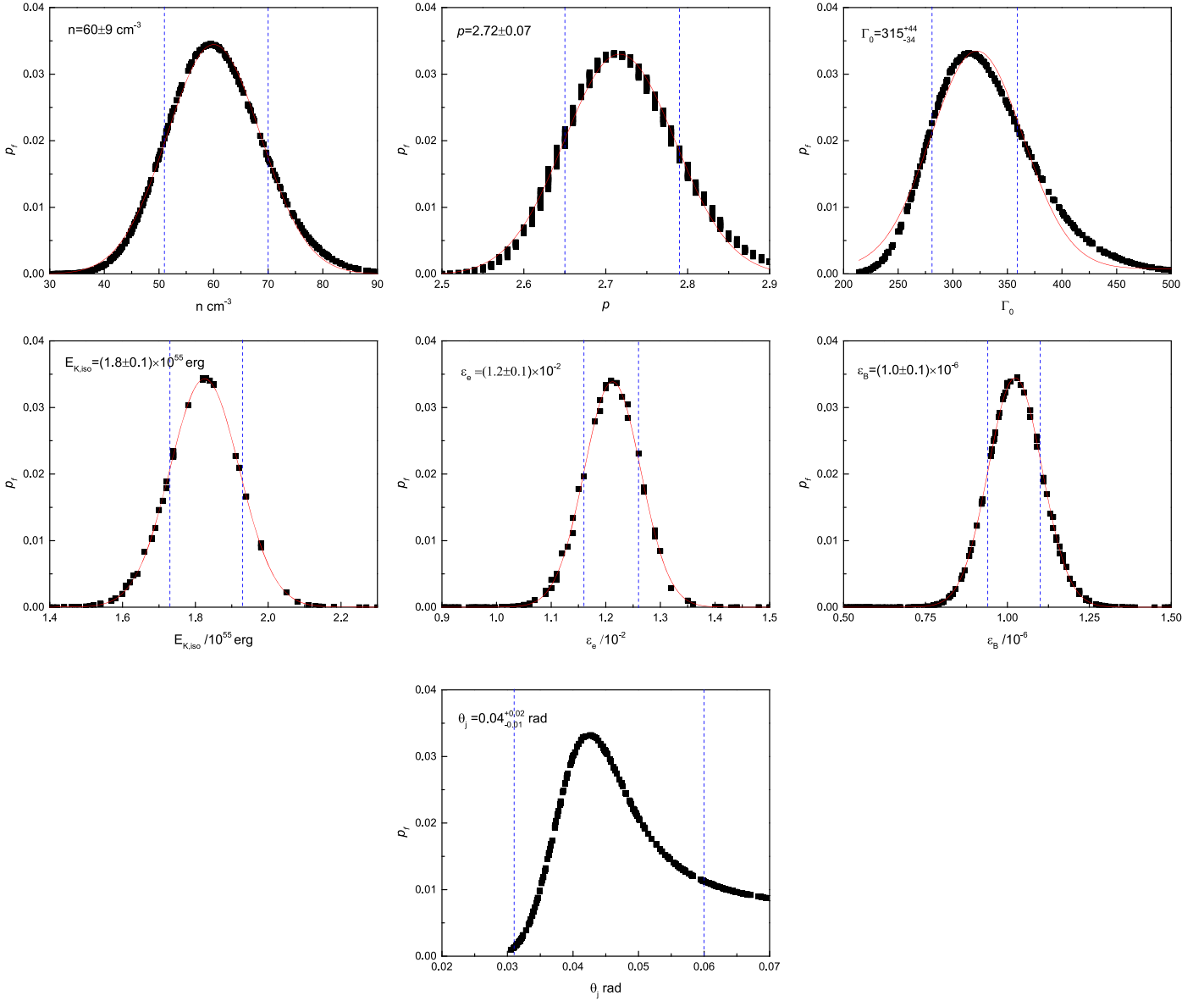
Figure 5. Probability distributions of the afterglow model parameters along with our Gaussian function fits (solid red lines) for GRB 140629A. The dashed vertical lines mark the 1σ confidence level of the parameters in this parameter set.

($n = 60\,\mathrm{cm}^{-3}$). In addition, the radiation efficiency of GRB 140629A is extremely low. We test whether or not it satisfies various empirical relations reported in the literature derived from observations of the prompt gamma-ray phase and the multi-wavelength afterglows. By estimating the jet opening angle with a jet-like break time t_j in late multi-wavelength light curves, Ghirlanda et al. (2004a) derived a tight correlation between geometrically corrected jet energy $E_{\gamma,j}$ and the peak energy E'_p of νf_ν spectrum in the burst frame, i.e., $E'_p = 267.0(E_{\gamma,j}/4.3 \times 10^{50}\,\mathrm{erg})^{0.706\pm0.047}$. The E'_p value inferred from the Ghirlanda relation is 46 keV for GRB 140629A, which is definitely inconsistent with the data, i.e., $E'_p \sim E_p \times (1+z) \sim 283$ keV. Liang & Zhang (2005) derived an empirical relation between $E_{\gamma,\mathrm{iso}}$, E'_p, and the jet break time (t'_j) in the burst frame, i.e., $E_{\gamma,\mathrm{iso}}/10^{52}\,\mathrm{erg} = (0.85 \pm 0.21) \times (E'_p/100\,\mathrm{keV})^{1.94\pm0.17} \times (t'_b/1\,\mathrm{day})^{-1.24\pm0.23}$.

Based on this relation, an isotropic energy $E_{\gamma,\mathrm{iso}} = 7.9 \times 10^{53}\,\mathrm{erg}$ is obtained, which is larger than that observed by more than one order of magnitude. These results suggest that GRB 140629A does not follow these two relations (Ghirlanda et al. 2004a; Liang & Zhang 2005), although both tight correlations have been used for measuring the cosmological parameters with GRBs (e.g., Dai et al. 2004; Ghirlanda et al. 2004b; Liang & Zhang 2005; Wang et al. 2015a). Note that the observed jet break time of GRB 140629A is much earlier, hence the inferred θ_j is much lower than those of the GRBs used to derive these relations (e.g., Frail et al. 2001; Bloom et al. 2003). It is unclear whether the violation of GRB 140629A is due to the selection effect or other physical reasons. For example, two-component jet models composed of a narrow and a wide component have been proposed to explain the data of some GRBs (e.g., Huang et al. 2004; Racusin et al. 2008). In these cases, the
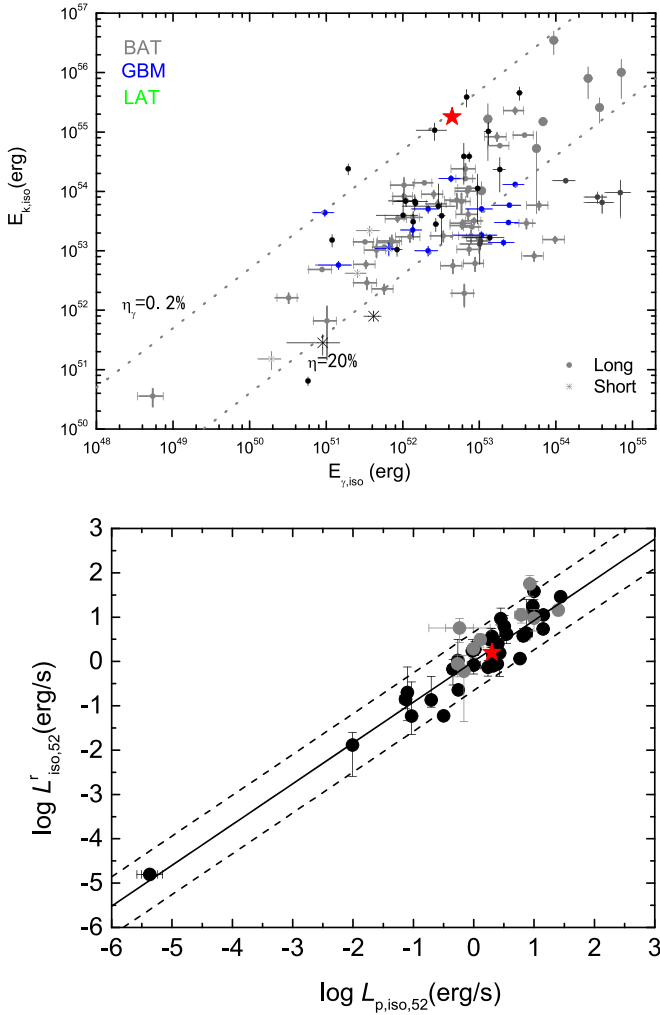
Figure 6. Top: comparison of GRB 140629A (the red star) with typical GRBs in the $E_{K,iso}-E_{\gamma,iso}$ plane. Bottom: illustration of the consistency of GRB 140629A with the tight $L_{\gamma,iso}-E'_p-\Gamma_0$ relation (Liang et al. 2015).

high-energy emission was proposed to be emitted by the narrow jet. However, one cannot exclude the possibility that the observed gamma-ray energy would be dominated by the wide jet component under certain conditions. Meanwhile, the early break time for GRB 140629A is likely due to the effect of the narrow jet component but not the wide one. If this is the case, the inconsistency between the jet energy and the opening angle would result in this violation of GRB 140629A. Liang et al. (2015) discovered a tight empirical correlation between L_{iso}, E'_p, and Γ_0 to reveal the direct connection between the gamma-ray and afterglows,

$$L_{iso,52} = 10^{-6.38 \pm 0.35}(E'_p/\text{keV})^{1.34 \pm 0.14}\Gamma_0^{1.32 \pm 0.19}. \quad (7)$$

Based on the equation above, we get $L_{iso,52} = 1.60^{+0.32}_{-0.30}$ for GRB 140629A, where the error is calculated from the uncertainties in E'_p and Γ_0 only. The derived $L_{iso,52}$ is well consistent with the observed one, 2.0×10^{52} erg s^{-1}, as shown in Figure 6. Note that the initial Lorentz factor of the ejecta Γ_0 is sensitive to the deceleration time (the peak time of the onset bump), but not strongly related to the jet break time. The onset of the afterglow bump is usually bright (Liang et al. 2010,

2013; Li et al. 2012; Wang et al. 2013), and it is easier to identify than the jet break time from an observed light curve.[10] The consistency of GRB 140629A with $L_{iso}-E'_p-\Gamma_0$ suggests that this relation is more robust than the Ghirlanda or Liang–Zhang relations, since it is not sensitive to the jet opening angle θ_j.

6. Conclusions

We have presented our optical photometric and spectroscopic observations of GRB 140629A with the TNT and the 2.16 m telescope at Xinglong Observatory. The redshift of GRB 140629A of $z = 2.275 \pm 0.043$ is measured through the metal absorption lines from our spectroscopic data. With the EWs of the lines C IVλ1549 and C IIλ1335 measured from our Gaussian fits to the line profiles, we obtain their ratio as 2.79 ± 0.49, indicating a high ionization level of the surrounding environment due to the GRB's radiation at the early phase after the burst. The optical–X-ray afterglow spectrum is jointly fitted with a single power-law function, yielding a photon index of -1.90 ± 0.05. The optical extinction and the neutral hydrogen absorption of the GRB host galaxy are negligible. We fit the optical and X-ray afterglow light curves using the forward shock model and find that it well represents the observed light curves with the following parameter set: $\Gamma_0 = 315^{+44}_{-34}$, $\epsilon_e = (1.2 \pm 0.1) \times 10^{-2}$, $\epsilon_B = (1.0 \pm 0.1) \times 10^{-6}$, $n = 60 \pm 9\,\text{cm}^{-3}$, $E_{K,iso} = (1.8 \pm 0.1) \times 10^{55}$ erg, $p = 2.72 \pm 0.07$, and $\theta_j = 0.04^{+0.02}_{-0.01}$ rad. The extremely low GRB radiation efficiency derived from our analysis agrees well with the prediction of the baryonic-dominated jet models. The extremely small opening angle allows GRB 140629A to confidently violate the Ghirlanda and Liang–Zhang relations. However, it still agrees well with the $L_{iso}-E'_p-\Gamma_0$ relation.

---

[10] The jet break is usually detected in late optical afterglow light curves. It is dim and also contaminated by emission from the host galaxy and/or associated supernovae (e.g., Li et al. 2012). This is also an issue in identifying an observed jet break as the narrow or the wide component in the case of a two-component jet.

ORCID iDs

Li-Ping Xin ⓘ https://orcid.org/0000-0002-9422-3437
En-Wei Liang ⓘ https://orcid.org/0000-0002-7044-733X

References

Adelman-McCarthy, J. K., Agüeros, M. A., Allam, S. S., et al. 2008, ApJS, 175, 297
Beuermann, K., Hessman, F. V., Reinsch, K., et al. 1999, A&A, 352, 26
Bikmaev, I., Khamitov, I., Irtuganov, E., et al. 2014, GCN, 16482, 1
Bloom, J. S., Frail, D. A., & Kulkarni, S. R. 2003, ApJ, 594, 674
Burrows, D. N., Kennea, J. A., Abbey, A. F., et al. 2007, Proc. SPIE, 6686, 668607
Cardelli, J. A., Clayton, G. C., & Mathis, J. S. 1989, ApJ, 345, 245
Cucchiara, A., Cenko, S. B., Bloom, J. S., et al. 2011, ApJ, 743, 154
Cummings, J. R., Barthelmy, S. D., Baumgartner, W. H., et al. 2014, GCN, 16481, 1
Dai, X., Halpern, J. P., Morgan, N. D., et al. 2007, ApJ, 658, 509
Dai, Z. G., Liang, E. W., & Xu, D. 2004, ApJL, 612, L101
Dai, Z. G., & Lu, T. 1998, MNRAS, 298, 87
Daigne, F., & Mochkovitch, R. 1998, MNRAS, 296, 275
D'Avanzo, P., Malesani, D., D'Elia, V., et al. 2014, GCN, 16493, 1
D'Elia, V., Fiore, F., Perna, R., et al. 2009, A&A, 503, 437
de Ugarte Postigo, A., Fynbo, J. P. U., Thöne, C. C., et al. 2012, A&A, 548, A11
Dessauges-Zavadsky, M., Chen, H.-W., Prochaska, J. X., Bloom, J. S., & Barth, A. J. 2006, ApJL, 648, L89
Evans, P. A., Beardmore, A. P., Page, K. L., et al. 2007, A&A, 469, 379
Evans, P. A., Beardmore, A. P., Page, K. L., et al. 2009, MNRAS, 397, 1177
Fan, Y., & Piran, T. 2006, MNRAS, 369, 197
Fan, Z., Wang, H., Jiang, X., et al. 2016, PASP, 128, 115005
Frail, D. A., Kulkarni, S. R., Sari, R., et al. 2001, ApJL, 562, L55
Gao, H., Lei, W.-H., Zou, Y.-C., Wu, X.-F., & Zhang, B. 2013, NewAR, 57, 141
Gao, H., Wang, X.-G., Mészáros, P., & Zhang, B. 2015, ApJ, 810, 160
Ghirlanda, G., Ghisellini, G., & Lazzati, D. 2004a, ApJ, 616, 331
Ghirlanda, G., Ghisellini, G., Lazzati, D., & Firmani, C. 2004b, ApJL, 613, L13
Golenetskii, S., Aptekar, R., Frederiks, D., et al. 2014, GCN, 16495, 1
Gorbovskoy, E., Krushinski, V., Pruzhinskaya, M., et al. 2014, GCN, 16500, 1
Harrison, F. A., Bloom, J. S., Frail, D. A., et al. 1999, ApJL, 523, L121
Hu, Y.-D., Liang, E.-W., Xi, S.-Q., et al. 2014, ApJ, 789, 145
Huang, X.-L., Xin, L.-P., Yi, S.-X., et al. 2016, ApJ, 833, 100
Huang, Y. F., Dai, Z. G., & Lu, T. 2000, MNRAS, 316, 943
Huang, Y. F., Wu, X. F., Dai, Z. G., Ma, H. T., & Lu, T. 2004, ApJ, 605, 300
Japelj, J., Kopač, D., Kobayashi, S., et al. 2014, ApJ, 785, 84
Kann, D. A., Klose, S., Zhang, B., et al. 2010, ApJ, 720, 1513
Kobayashi, S., Piran, T., & Sari, R. 1997, ApJ, 490, 92
Kobayashi, S., & Zhang, B. 2007, ApJ, 655, 973
Kriss, G. 1994, ASPC, 61, 437
Kumar, P. 1999, ApJL, 523, L113
Kumar, P., & Zhang, B. 2015, PhR, 561, 1
Kuroda, D., Hanayama, H., Miyaji, T., et al. 2014, GCN, 16488, 1
Li, L., Liang, E.-W., Tang, Q.-W., et al. 2012, ApJ, 758, 27
Liang, E., & Zhang, B. 2005, ApJ, 633, 611
Liang, E.-W., Li, L., Gao, H., et al. 2013, ApJ, 774, 13
Liang, E.-W., Lin, T.-T., Lü, J., et al. 2015, ApJ, 813, 116
Liang, E.-W., Lü, H.-J., Hou, S.-J., Zhang, B.-B., & Zhang, B. 2009, ApJ, 707, 328
Liang, E.-W., Racusin, J. L., Zhang, B., Zhang, B.-B., & Burrows, D. N. 2008, ApJ, 675, 528
Liang, E.-W., Yi, S.-X., Zhang, J., et al. 2010, ApJ, 725, 2209
Liang, E.-W., Zhang, B.-B., & Zhang, B. 2007, ApJ, 670, 565
Liang, E. W., Zhang, B., O'Brien, P. T., et al. 2006, ApJ, 646, 351
Lien, A. Y., Barthelmy, S. D., Bernardini, M. G., et al. 2014, GCN, 16477, 1
Maehara, H. 2014, GCN, 16484, 1
Malesani, D. 2014, GCN, 16485, 1
Masi, G. 2014, GCN, 16483, 1
Massey, P., Strobel, K., Barnes, J. V., & Anderson, E. 1988, ApJ, 328, 315
Mészáros, P. 2006, RPPh, 69, 2259
Moskvitin, A., Burenin, R., Uklein, R., et al. 2014a, GCN, 16489, 1
Moskvitin, A., Burenin, R., Uklein, R., Sokolov, V., & Sokolova, T. 2014b, GCN, 16499, 1
Moskvitin, A. S., Komarova, V. N., Sokolova, T. N., & Sokolov, V. V. 2014c, GCN, 16518, 1
Mu, H.-J., Lin, D.-B., Xi, S.-Q., et al. 2016, ApJ, 831, 111
Nakar, E., & Granot, J. 2007, MNRAS, 380, 1744
Nicuesa Guelbenzu, A., Klose, S., Rossi, A., et al. 2011, A&A, 531, L6
Nousek, J. A., Kouveliotou, C., Grupe, D., et al. 2006, ApJ, 642, 389
Oates, S. R., Page, M. J., Schady, P., et al. 2009, MNRAS, 395, 490
O'Brien, P. T., Willingale, R., Osborne, J., et al. 2006, ApJ, 647, 1213
Panaitescu, A. 2005, MNRAS, 362, 921
Panaitescu, A., & Kumar, P. 2002, ApJ, 571, 779
Panaitescu, A., Mészáros, P., Burrows, D., et al. 2006, MNRAS, 369, 2059
Panaitescu, A., Spada, M., & Mészáros, P. 1999, ApJL, 522, L105
Panaitescu, A., & Vestrand, W. T. 2011, MNRAS, 414, 3537
Peng, F.-K., Liang, E.-W., Wang, X.-Y., et al. 2014, ApJ, 795, 155
Perley, D. A., & Cenko, S. B. 2014, GCN, 16491, 1
Piran, T. 1999, PhR, 314, 575
Qin, Y., Liang, E.-W., Liang, Y.-F., et al. 2013, ApJ, 763, 15
Racusin, J. L., Karpov, S. V., Sokolowski, M., et al. 2008, Natur, 455, 183
Rhoads, J. E. 1999, ApJ, 525, 737
Santana, R., Barniol Duran, R., & Kumar, P. 2014, ApJ, 785, 29
Sari, R., & Piran, T. 1999, ApJ, 520, 641
Sari, R., Piran, T., & Narayan, R. 1998, ApJL, 497, L17
Schlegel, D. J., Finkbeiner, D. P., & Davis, M. 1998, ApJ, 500, 525
Sonbas, E., Dolek, F., Guver, T., et al. 2014, GCN, 16486, 1
Swenson, C. A., Roming, P. W. A., De Pasquale, M., & Oates, S. R. 2013, ApJ, 774, 2
Vreeswijk, P. M., Ledoux, C., Smette, A., et al. 2007, A&A, 468, 83
Wang, F. Y., Dai, Z. G., & Liang, E. W. 2015a, NewAR, 67, 1
Wang, X.-G., Liang, E.-W., Li, L., et al. 2013, ApJ, 774, 132
Wang, X.-G., Zhang, B., Liang, E.-W., et al. 2015b, ApJS, 219, 9
Wijers, R. A. M. J., & Galama, T. J. 1999, ApJ, 523, 177
Xin, L.-P., Liang, E.-W., Wei, J.-Y., et al. 2011, MNRAS, 410, 27
Xin, L.-P., Wang, Y.-Z., Lin, T.-T., et al. 2016b, ApJ, 817, 152
Xin, L.-P., Wei, J.-Y., Qiu, Y.-L., et al. 2016a, RAA, 16, 012
Yi, S.-X., Wu, X.-F., & Dai, Z.-G. 2013, ApJ, 776, 120
Yost, S. A., Harrison, F. A., Sari, R., & Frail, D. A. 2003, ApJ, 597, 459
Yurkov, V., Sergienko, Y., Varda, D., et al. 2014, GCN, 16478, 1
Zhang, B., Fan, Y. Z., Dyks, J., et al. 2006, ApJ, 642, 354
Zhang, B., & Mészáros, P. 2002, ApJ, 566, 712
Zhang, B., & Mészáros, P. 2004, IJMPA, 19, 2385
Zhang, B.-B., Liang, E.-W., & Zhang, B. 2007, ApJ, 666, 1002
Zheng, W.-K., Deng, J.-S., Zhai, M., et al. 2008, ChJAA, 8, 693